



Millinovae: A New Class of Transient Supersoft X-Ray Sources without a Classical Nova Eruption

Przemek Mróz¹ , Krzysztof Król¹ , Hélène Szegedi² , Philip Charles^{2,3} , Kim L. Page⁴ , Andrzej Udalski¹ , David A. H. Buckley^{2,5,6} , Gulab Dewangan⁷ , Pieter Meintjes² , Michał K. Szymański¹ , Igor Soszyński¹ , Paweł Pietrukowicz¹ , Szymon Kozłowski¹ , Radosław Poleski¹ , Jan Skowron¹ , Krzysztof Ulaczyk^{1,8} , Mariusz Gromadzki¹ , Krzysztof Rybicki^{1,9} , Patryk Iwanek¹ , Marcin Wrona^{1,10} , and Mateusz J. Mróz¹

¹ Astronomical Observatory, University of Warsaw, Al. Ujazdowskie 4, 00-478 Warszawa, Poland; pmroz@astrouw.edu.pl

² Department of Physics, University of the Free State, 205 Nelson Mandela Drive, Bloemfontein, 9300, South Africa

³ Department of Physics and Astronomy, University of Southampton, Southampton, Hampshire SO17 1BJ, UK

⁴ School of Physics and Astronomy, University of Leicester, Leicester LE1 7RH, UK

⁵ South African Astronomical Observatory, PO Box 9, Observatory Road, Observatory 7935, South Africa

⁶ Department of Astronomy, University of Cape Town, Private Bag X3, Rondebosch 7701, South Africa

⁷ Inter-University Centre for Astronomy & Astrophysics, Post Bag 4, Ganeshkhind, Pune, Maharashtra 411007, India

⁸ Department of Physics, University of Warwick, Coventry CV4 7 AL, UK

⁹ Department of Particle Physics and Astrophysics, Weizmann Institute of Science, Rehovot 76100, Israel

¹⁰ Department of Astrophysics and Planetary Sciences, Villanova University, 800 Lancaster Avenue, Villanova, PA 19085, USA

Received 2024 September 25; revised 2024 November 20; accepted 2024 November 23; published 2024 December 12

Abstract

Some accreting binary systems containing a white dwarf (such as classical novae or persistent supersoft sources) are seen to emit low-energy X-rays with temperatures of $\sim 10^6$ K and luminosities exceeding 10^{35} erg s⁻¹. These X-rays are thought to originate from nuclear burning on the white dwarf surface, either caused by a thermonuclear runaway (classical novae) or a high mass-accretion rate that sustains steady nuclear burning (persistent sources). The discovery of transient supersoft X-rays from ASASSN-16oh challenged these ideas, as no clear signatures of mass ejection indicative of a classical nova eruption were detected, and the origin of these X-rays remains controversial. It was unclear whether this star was one of a kind or representative of a larger, as yet undiscovered, group. Here, we present the discovery of 29 stars located in the direction of the Magellanic Clouds exhibiting long-duration, symmetrical optical outbursts similar to that seen in ASASSN-16oh. We observed one of these objects during an optical outburst and found it to be emitting transient supersoft X-rays, while no signatures of mass ejection (indicative of a classical nova eruption) were detected. We therefore propose that these objects form a homogeneous group of transient supersoft X-ray sources, which we dub “millinovae” because their optical luminosities are approximately a 1000 times fainter than those of ordinary classical novae.

Unified Astronomy Thesaurus concepts: Cataclysmic variable stars (203); Classical novae (251); Dwarf novae (418)

1. Introduction

A classical nova eruption occurs on the surface of a white dwarf that is accreting matter from its nondegenerate companion via an accretion disk. A layer of fresh, usually hydrogen-rich gas accumulates on the white dwarf surface and becomes degenerate. The gas is heated, and when hydrogen ultimately ignites, a thermonuclear runaway ejects about 10^{-5} – $10^{-4} M_{\odot}$ of matter from the system with velocities from hundreds to thousands of km s⁻¹ (M. F. Bode & A. Evans 2008). As the ejecta expands and becomes optically thin, the exposed white dwarf surface is observed to emit supersoft X-rays due to stable hydrogen burning of the leftover gas (J. P. Osborne 2015; K. L. Page & A. W. Shaw 2022). The maximum X-ray luminosities of classical novae are typically 10^{36} – 10^{38} erg s⁻¹ (e.g., M. Henze et al. 2014). In the optical passbands, they normally reach absolute magnitudes from -6 to -10 (M. F. Bode & A. Evans 2008).

The accretion disk surrounding the white dwarf is subject to a thermal instability that can lead to dwarf nova outbursts. They

occur when gas in the disk reaches a critical temperature, and its viscosity abruptly changes, increasing the mass accretion rate onto the white dwarf (J.-P. Lasota 2001). If the instability develops in the outer regions of the accretion disk (outside-in outbursts), the rise to maximum brightness is rapid. However, the light curves of inside-out outbursts (which start in the inner disk regions) are more symmetric, with a relatively slow rise to the peak (J.-P. Lasota 2001). Dwarf novae in outburst reach optical absolute magnitudes from $+6$ to 0 , depending on their orbital period (longer orbital periods mean larger accretion disks, and hence, they become brighter; J. Patterson 2011). The X-ray luminosities of dwarf novae in outbursts are typically 10^{29} – 10^{32} erg s⁻¹, about 6 orders of magnitude lower than those of classical novae (A. D. Schwope et al. 2024; A. C. Rodriguez et al. 2024).

Therefore, the discovery of supersoft X-ray emission from the optical transient ASASSN-16oh (T. J. Maccarone et al. 2019) was a surprise. The X-ray emission was consistent with that of a $\sim 900,000$ K blackbody and a luminosity of about 6.7×10^{36} erg s⁻¹, similar to that seen from persistent supersoft X-ray sources and classical novae. However, the optical properties of the transient (light-curve shape, its amplitude, peak absolute magnitude, and optical spectra) did not match those of classical novae at all.



Original content from this work may be used under the terms of the [Creative Commons Attribution 4.0 licence](https://creativecommons.org/licenses/by/4.0/). Any further distribution of this work must maintain attribution to the author(s) and the title of the work, journal citation and DOI.

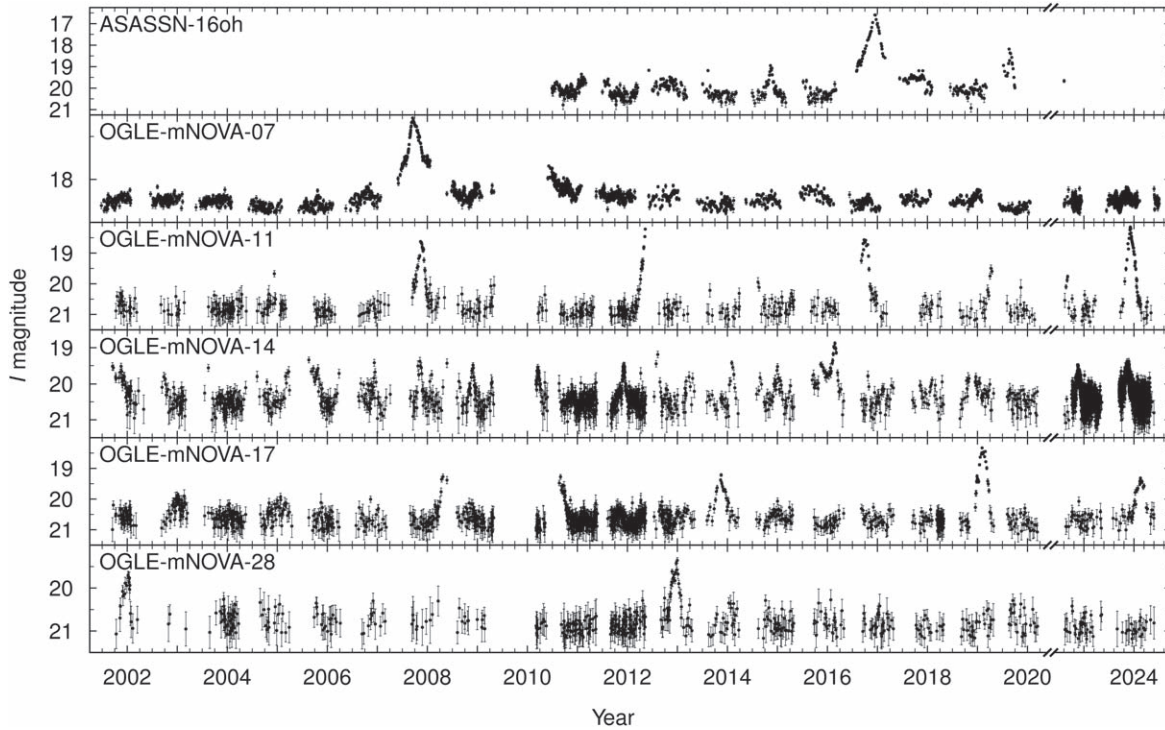


Figure 1. Example light curves of millinovae. The upper panel shows the prototype, ASASSN-16oh. The y-axis ticks are every 0.5 mag. There is a gap in the data between 2020.4 and 2022.4.

ASASSN-16oh was first detected in 2016 December by the All-Sky Automated Survey for Supernovae (ASASSN; B. J. Shappee et al. 2014) as a $V = 16.9$ transient in the Small Magellanic Cloud (SMC). Its archival light curve (upper panel of Figure 1) collected by the Optical Gravitational Lensing Experiment (OGLE; A. Udalski et al. 2015) revealed that the optical outburst commenced at least 4 months before the ASASSN discovery. The object exhibited irregular variability before (and after) the outburst, with a mean brightness of about $I = 20.3$ and $V = 21.1$. It peaked at $I \approx 16.6$, which corresponds to $M_I = -2.5 \pm 0.1$, assuming the SMC distance modulus of $\mu = 18.977 \pm 0.016$ (D. Graczyk et al. 2020) and reddening of $E(V - I) = 0.059^{+0.052}_{-0.045}$ (D. M. Skowron et al. 2021). The full optical light curve does not match those of classical novae, which normally rise to maximum within hours to a few days (not months). Additionally, the optical spectra revealed narrow (FWHM = 164 km s^{-1}) Balmer and He II emission lines (T. J. Maccarone et al. 2019), unlike the broad features (several hundred to a few thousand km s^{-1}) usually observed in classical novae.

The unusual outburst light curve, narrow optical emission lines, and X-ray spectrum led T. J. Maccarone et al. (2019) to propose that the X-rays come from a spreading layer—a belt around the white dwarf’s equator near the inner disk edge in which a large fraction of the total accretion energy is emitted. However, this interpretation remains controversial, with alternative models being based on a nonejecting nova outburst (Y. Hillman et al. 2019; M. Kato et al. 2020).

Y. Hillman et al. (2019) proposed that both the optical flux and X-ray emission in ASASSN-16oh originated from a hot white dwarf that underwent a non-mass-ejecting thermonuclear runaway. They argued that such nonejecting nova events are possible if the mass accretion rate onto the white dwarf is sufficiently high (at least a few times $10^{-7} M_{\odot} \text{ yr}^{-1}$) and

claimed that the light curve of ASASSN-16oh is best modeled by a $1.1 M_{\odot}$ white dwarf accreting at $3.5\text{--}5 \times 10^{-7} M_{\odot} \text{ yr}^{-1}$. Nonetheless, their model predicted an asymmetric outburst (with a rapid rise to the peak followed by a slower decline), in stark contrast to observations. Furthermore M. Kato et al. (2020) later criticized this model, pointing out that Hillman et al. had overestimated the optical brightness by 6 mag.

On the other hand, M. Kato et al. (2020) proposed that the outburst of ASASSN-16oh was triggered by a sudden mass accretion caused by disk instability. In this model, the optical flux originates from the irradiated accretion disk, and X-rays are coming from the hot hydrogen-burning white dwarf surface. They found that the X-ray light curve of ASASSN-16oh is best explained by a massive ($1.32 M_{\odot}$) white dwarf model.

Given the unusual and unexplained optical and X-ray properties of ASASSN-16oh, we decided to investigate whether this star is one of a kind or representative of a larger, as yet undiscovered, group. We thus searched for objects with outburst properties similar to those seen in ASASSN-16oh among the 20 yr-long light curves of 76 million stars observed toward the Magellanic Clouds by the OGLE survey (A. Udalski et al. 2015).

2. OGLE Photometric Data

The OGLE photometric data have been collected using the 1.3 m Warsaw Telescope located at Las Campanas Observatory, Chile, during the OGLE-III (2001–2009; A. Udalski 2003) and OGLE-IV (2010–2024; A. Udalski et al. 2015) phases of the project. Different instruments were used in different phases of the survey. The OGLE-III camera consisted of eight 2048×4096 CCD detectors, with a plate scale of $0.26 \text{ arcsec pixel}^{-1}$. The OGLE-IV camera had the same pixel scale but comprised thirty-two 2048×4102 detectors,

Table 1
List of Detected Objects

Name	R.A. (hh:mm:ss)	Decl. (deg:arcmin:arcsec)	I_q (mag)	$(V - I)_q$ (mag)	I_{\max} (mag)	$(V - I)_{\max}$ (mag)	ΔI (mag)	ΔT (day)	τ_d (day mag ⁻¹)	$E(V - I)$ (mag)	Comments
OGLE-mNOVA-01	01: 57: 43.64	-73: 37: 32.5	20.273 \pm 0.016	0.784 \pm 0.056	16.595 \pm 0.012	0.198 \pm 0.008	3.7	> 200	33	0.059	ASASSN-16oh
OGLE-mNOVA-02	00: 20: 40.41	-75: 11: 56.5	20.981 \pm 0.017	1.088 \pm 0.058	19.216 \pm 0.050	...	1.8	> 70	...	0.042	...
OGLE-mNOVA-03	00: 26: 10.69	-73: 34: 18.2	21.063 \pm 0.040	0.502 \pm 0.186	19.956 \pm 0.055	0.501 \pm 0.055	1.1	55	33	0.028	...
OGLE-mNOVA-04	00: 34: 30.23	-74: 05: 40.3	21.008 \pm 0.025	0.611 \pm 0.239	19.706 \pm 0.064	...	1.3	83	26	0.046	...
OGLE-mNOVA-05	00: 50: 08.58	-69: 46: 33.8	20.745 \pm 0.017	0.894 \pm 0.068	18.885 \pm 0.022	0.420 \pm 0.017	1.9	74	39	0.016	candidate
OGLE-mNOVA-06	00: 51: 18.58	-68: 54: 34.7	20.916 \pm 0.017	1.051 \pm 0.073	19.268 \pm 0.029	0.354 \pm 0.033	1.6	102	20	0.011	...
OGLE-mNOVA-07	00: 52: 45.30	-72: 20: 07.5	18.276 \pm 0.010	0.574 \pm 0.015	17.301 \pm 0.012	0.545 \pm 0.008	1.0	> 235	213	0.068	...
OGLE-mNOVA-08	04: 51: 40.68	-68: 25: 14.5	20.197 \pm 0.013	0.987 \pm 0.019	18.255 \pm 0.024	...	1.9	78	27	0.128	...
OGLE-mNOVA-09	04: 51: 58.14	-68: 30: 35.6	20.057 \pm 0.015	1.428 \pm 0.064	19.015 \pm 0.046	1.267 \pm 0.028	1.0	115	105	0.122	candidate
OGLE-mNOVA-10	04: 56: 24.20	-68: 27: 31.5	20.673 \pm 0.026	0.789 \pm 0.110	19.586 \pm 0.091	0.771 \pm 0.128	1.1	80	41	0.119	...
OGLE-mNOVA-11	04: 59: 56.68	-67: 31: 48.9	20.884 \pm 0.039	1.244 \pm 0.129	18.151 \pm 0.021	0.420 \pm 0.023	2.7	142	29	0.100	...
OGLE-mNOVA-12	05: 04: 03.38	-69: 33: 17.9	20.814 \pm 0.033	0.776 \pm 0.171	19.407 \pm 0.029	0.570 \pm 0.014	1.4	95	65	0.083	MACHO-LMC-7
OGLE-mNOVA-13	05: 06: 17.46	-70: 58: 46.8	20.096 \pm 0.011	0.847 \pm 0.018	18.909 \pm 0.048	...	1.2	131	30	0.124	MACHO-LMC-23
OGLE-mNOVA-14	05: 10: 15.41	-70: 31: 43.6	20.423 \pm 0.018	0.372 \pm 0.061	18.847 \pm 0.058	0.156 \pm 0.091	1.6	95	17	0.092	...
OGLE-mNOVA-15	05: 12: 44.80	-69: 41: 28.0	20.790 \pm 0.022	0.886 \pm 0.078	18.540 \pm 0.018	0.478 \pm 0.015	2.2	> 120	34	0.183	candidate
OGLE-mNOVA-16	05: 14: 22.96	-70: 56: 56.1	20.545 \pm 0.019	0.327 \pm 0.031	19.202 \pm 0.045	0.223 \pm 0.061	1.3	42	24	0.072	...
OGLE-mNOVA-17	05: 15: 05.58	-68: 31: 07.2	20.461 \pm 0.015	0.893 \pm 0.087	19.312 \pm 0.065	0.810 \pm 0.027	1.1	120	49	0.105	...
OGLE-mNOVA-18	05: 15: 17.91	-70: 36: 58.6	20.366 \pm 0.011	0.904 \pm 0.018	18.570 \pm 0.037	0.756 \pm 0.078	1.8	105	58	0.094	...
OGLE-mNOVA-19	05: 17: 12.72	-68: 49: 38.4	21.179 \pm 0.031	0.838 \pm 0.084	19.775 \pm 0.037	0.541 \pm 0.045	1.4	48	21	0.102	...
OGLE-mNOVA-20	05: 20: 05.81	-69: 38: 31.0	19.648 \pm 0.011	0.118 \pm 0.018	18.259 \pm 0.020	0.146 \pm 0.024	1.4	108	35	0.078	...
OGLE-mNOVA-21	05: 25: 58.44	-69: 34: 33.8	19.886 \pm 0.011	0.656 \pm 0.017	18.492 \pm 0.025	0.498 \pm 0.020	1.4	> 110	39	0.078	...
OGLE-mNOVA-22	05: 26: 45.21	-70: 29: 45.7	18.574 \pm 0.010	0.580 \pm 0.014	17.653 \pm 0.015	...	0.9	> 800	...	0.139	...
OGLE-mNOVA-23	05: 27: 48.98	-68: 15: 44.6	21.167 \pm 0.047	0.700 \pm 0.302	20.006 \pm 0.051	0.451 \pm 0.029	1.2	33	14	0.099	...
OGLE-mNOVA-24	05: 28: 25.12	-70: 20: 43.8	21.032 \pm 0.048	0.671 \pm 0.094	18.661 \pm 0.036	0.487 \pm 0.027	2.4	> 280	48	0.082	...
OGLE-mNOVA-25	05: 30: 47.88	-69: 54: 33.8	20.404 \pm 0.014	0.428 \pm 0.022	19.228 \pm 0.080	0.520 \pm 0.059	1.2	81	39	0.060	OGLE-LMC-02
OGLE-mNOVA-26	05: 32: 10.63	-70: 22: 09.5	20.764 \pm 0.027	0.097 \pm 0.116	19.366 \pm 0.057	-0.023 \pm 0.025	1.4	43	148	0.124	...
OGLE-mNOVA-27	05: 37: 56.29	-68: 48: 51.0	20.763 \pm 0.028	1.010 \pm 0.025	19.273 \pm 0.069	...	1.5	40	14	0.263	...
OGLE-mNOVA-28	05: 52: 29.30	-71: 10: 29.9	20.818 \pm 0.023	1.079 \pm 0.227	19.439 \pm 0.034	0.537 \pm 0.055	1.4	85	26	0.141	...
OGLE-mNOVA-29	05: 53: 41.54	-70: 22: 23.0	20.747 \pm 0.019	0.410 \pm 0.027	19.758 \pm 0.078	0.655 \pm 0.088	1.0	> 120	...	0.105	...

Note. The table provides equatorial coordinates (for the epoch J2000), mean I -band brightness and $V - I$ color in quiescence, mean I -band brightness and $V - I$ color in outburst, amplitude of the outburst in I -band ΔI , duration of the highest-amplitude outburst ΔT , mean decline rate τ_d , and color excess $E(V - I)$ (D. M. Skowron et al. 2021) toward the detected objects.

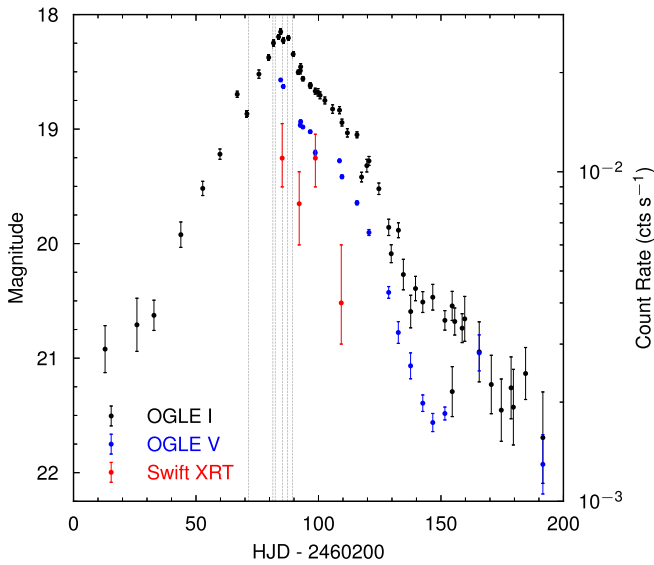


Figure 2. Photometric and X-ray observations of the 2023/2024 outburst of OGLE-mNOVA-11. Dotted lines mark times of SALT spectroscopic observations.

providing a field of view of 1.4 deg^2 . The typical exposure time was 150 s. The photometric data were extracted using a custom version of the difference image analysis algorithm (A. B. Tomaney & A. P. S. Crotts 1996; C. Alard & R. H. Lupton 1998) implemented by P. R. Woźniak (2000). The OGLE-III and OGLE-IV data have been reduced using the same reference image (P. Mróz et al. 2024), enabling us to obtain homogeneous, long-term light curves of all analyzed objects. Photometry was calibrated to the standard I - and V -band systems. See A. Udalski (2003) and A. Udalski et al. (2015) for a detailed description of the observing setup and data calibration. All data presented in this Letter are available to the astronomical community from <https://ftp.astrouw.edu.pl/ogle/ogle4/millinovae/>.

3. Results

We started with a list of 72,303 objects (54,996 in the Large Magellanic Cloud, LMC, and 17,307 in the SMC) whose light curves contain at least five consecutive data points magnified with respect to the remaining light curve (see P. Mróz et al. 2024 for more details about the selection of outbursting events). We required that the light curve contain at least one outburst with an amplitude larger than 1 mag and duration between 10 and 600 days. Subsequently, we cross-matched selected objects with the Gaia Data Release 3 (DR3) archive (Gaia Collaboration et al. 2023) and removed artifacts due to high-proper-motion stars (those with proper motions $> 10 \text{ mas yr}^{-1}$), which were the largest source of contamination. The light curves of the remaining objects (7412 in the LMC and 2689 in the SMC) were visually inspected, and we selected the initial sample of objects with triangle-shaped, symmetrical outbursts similar to those of ASASSN-16oh.

We vetted all selected objects using additional data, including multicolor photometry, Gaia parallaxes and proper motions, and sky images. We removed objects that could be classified as classical novae, supernovae, and active galactic nuclei, leaving us with a list of 29 objects (22 in the LMC and seven in the SMC). Example light curves are presented in

Figure 1 (see also Figures A1 and A2 in Appendix A). All objects show long-duration (weeks to months), symmetrical (triangle-shaped) outbursts with amplitudes in I ranging from 1.0 to 3.7 mag. Some outbursts are deceptively symmetric, which led to them being classified as gravitational microlensing events (OGLE-mNOVA-12 = MACHO-LMC-7 and OGLE-mNOVA-13 = MACHO-LMC-23, C. Alcock et al. 2000; OGLE-mNOVA-25 = OGLE-LMC-02, Ł. Wyrzykowski et al. 2009) although such events should be achromatic and nonrepeating if they really are due to microlensing. The list of all our selected objects is presented in Table 1.

Given the unique spectral and X-ray characteristics of ASASSN-16oh, we also decided to start the near-real-time monitoring of these selected objects in 2023 September, with the goal of triggering follow-up observations should any enter an outburst state.

4 Outburst of OGLE-mNOVA-11

The outburst of OGLE-mNOVA-11 started shortly afterwards, between 2023 October 15.3 and 26.3 and reached a maximum of $I = 18.15 \pm 0.02$ and $V = 18.57 \pm 0.01$ on 2023 December 6.1 (Figure 2), an amplitude of almost 3 mag. This corresponds to $M_I = -0.5 \pm 0.1$ and $M_V = -0.2 \pm 0.1$, assuming the LMC distance modulus of $\mu = 18.477 \pm 0.004$ (G. Pietrzyński et al. 2019) and reddening $E(V - I) = 0.100^{+0.065}_{-0.044}$ (D. M. Skowron et al. 2021). The star returned to quiescence (in I) in late 2024 February, about 120 days after the outburst onset. The outburst duration was shorter in V .

We obtained a set of low-resolution spectra of OGLE-mNOVA-11 from 2023 November 22 to December 10 (Figure 3) with the Robert Stobie Spectrograph (H. A. Kobulnicky et al. 2003; E. B. Burgh et al. 2003) mounted on the Southern African Large Telescope (SALT), as part of the SALT Large Science Programme on Transients (Appendix B). The spectra cover the range $3500\text{--}6700 \text{ Å}$ and reveal narrow ($\text{FWHM} = 247 \pm 28 \text{ km s}^{-1}$) emission lines (Balmer lines, He II 4686 Å). The Bowen blend (a complex of C III and N III lines in the range $4640\text{--}4650 \text{ Å}$) is also clearly detected from 2023 December 2 to 10. The emission lines are redshifted with a mean radial velocity of $278.3 \pm 4.5 \text{ km s}^{-1}$, close to that of the LMC systemic value ($262.2 \pm 3.4 \text{ km s}^{-1}$; R. P. van der Marel et al. 2002). Both the light-curve shape and optical spectra are very different from those of classical novae.

OGLE-mNOVA-11 was also observed by the Neil Gehrels Swift Observatory (N. Gehrels et al. 2004) five times from 2023 December 6 to 30 (Appendix C). Swift's X-Ray Telescope (XRT; D. N. Burrows et al. 2005) detected a faint X-ray source at the transient's position, with a $0.3\text{--}10 \text{ keV}$ count rate declining from $0.011^{+0.003}_{-0.002} \text{ count s}^{-1}$ (December 6) to $0.004^{+0.002}_{-0.001} \text{ count s}^{-1}$ (December 30); see Figure 2. All the data were combined to create a single X-ray spectrum, which can be fitted with a blackbody of $418,000^{+220,000}_{-130,000} \text{ K}$ absorbed by a column density $N_H = 3.5^{+13.0}_{-3.0} \times 10^{21} \text{ cm}^{-2}$. If we fix N_H to the LMC value ($1.3 \times 10^{21} \text{ cm}^{-2}$), then the temperature is slightly better constrained to $607,000^{+160,000}_{-130,000} \text{ K}$. Assuming this blackbody model, the observed L_X ($0.3\text{--}10 \text{ keV}$) $\approx 0.9 \times 10^{35} \text{ erg s}^{-1}$, or $3.6 \times 10^{35} \text{ erg s}^{-1}$ when corrected for absorption, about an order of magnitude smaller than that of ASASSN-16oh, but still substantially higher than dwarf nova X-ray luminosities.

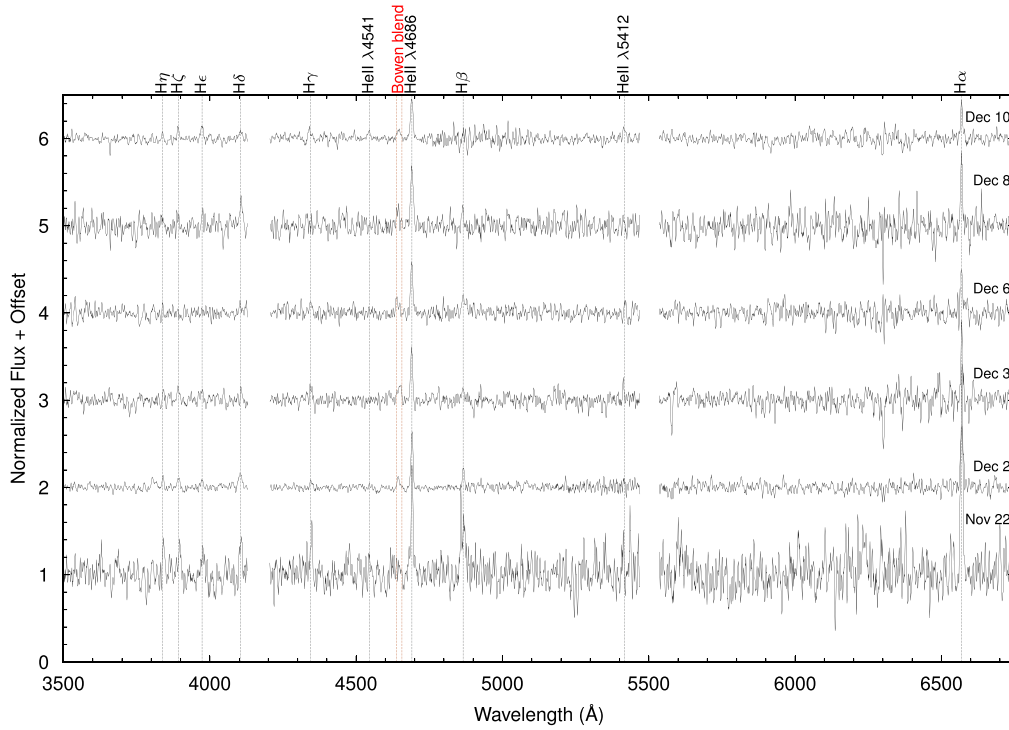


Figure 3. SALT spectroscopic observations of the 2023/2024 outburst of OGLE-mNOVA-11 reveal narrow emission lines, including He II (4686 Å) and Bowen blend.

5 Discussion and Conclusions

Overall, the optical (light-curve shape, narrow emission lines, strong He II emission) and X-ray properties of OGLE-mNOVA-11 match well with those of ASASSN-16oh. We thus propose that they, and probably the remaining objects described in this study, form a homogeneous group of transient supersoft X-ray sources. We dub them “millinovae” because their optical luminosities are roughly a 1000 times fainter than those of ordinary classical novae.¹¹

Using ASASSN-16oh and OGLE-mNOVA-11 as prototypes, millinovae should fulfill the following criteria:

1. They exhibit symmetrical, triangle-shaped outbursts in the optical bands (V , I).
2. Outbursts last from a month to several months, i.e., substantially longer than the typical outbursts of short-orbital-period dwarf novae.
3. The peak absolute magnitude in the optical bands is between that of classical novae and short-orbital-period dwarf novae.
4. The optical spectra show narrow (FWHM smaller than a few hundred km s^{-1}) emission lines of H and He II (that is, no signatures of mass ejection are seen in the spectra).
5. Soft X-ray emission (declining with decreasing optical luminosity) is seen during the outburst.

Only two systems (ASASSN-16oh and OGLE-mNOVA-11) meet all these five criteria. The remaining objects, given the lack of dedicated spectroscopic and X-ray observations during outbursts, remain millinova candidates.

Their sky location (upper panels of Figure 4) and the fact that most of the selected stars occupy a relatively narrow region in the color–magnitude diagram (middle left panel of Figure 4) indicate that millinovae are all in the Magellanic Clouds. We used the long-term astrometric time series of OGLE observations to measure proper motions of selected objects (Appendix D), which are consistent (with one exception) with those of stars located in the Magellanic Clouds (Gaia Collaboration et al. 2018). The radial velocities of ASASSN-16oh (T. J. Maccarone et al. 2019) and OGLE-mNOVA-11 (Appendix B) are consistent with the systemic velocities of the SMC and LMC, respectively. However, we cannot rule out that some objects are located in the foreground Milky Way disk or in background galaxies although we consider this very unlikely.

The middle left panel of Figure 4 shows that most objects in quiescence occupy the same region of the color–magnitude diagram, $0.5 \leq (V - I)_0 \leq 1.0$, $1.5 \leq M_I \leq 2.5$, which indicates that the accretion disk dominates their quiescent luminosity. Such a range is consistent with the absolute magnitudes of dwarf novae in the Magellanic Clouds (M. M. Shara et al. 2003), indicating that they are essentially nova-like disks. In outburst (middle right panel of Figure 4), objects move toward bluer colors ($0.0 \leq (V - I)_0 \leq 0.5$) and higher luminosities ($-0.5 < M_I < 1.0$), as expected given the strong irradiation of the disk by the supersoft component.

The mean absolute magnitudes of millinovae in quiescence are $M_I = 1.72 \pm 0.70$ and $M_V = 2.37 \pm 0.80$. In outburst, the absolute magnitudes are $M_I = 0.18 \pm 0.83$ and $M_V = 0.62 \pm 0.97$ and are about a 1000 times fainter than classical novae (lower right panel of Figure 4). Millinovae are also much brighter than most known dwarf novae (lower panels of Figure 4).

The spectroscopic properties of ASASSN-16oh and OGLE-mNOVA-11 and the $(V - I)$ color evolution of

¹¹ They should not be confused with “micronovae,” a much lower-luminosity and much faster event seen in a number of Galactic magnetic cataclysmic variables (S. Scaringi et al. 2022).

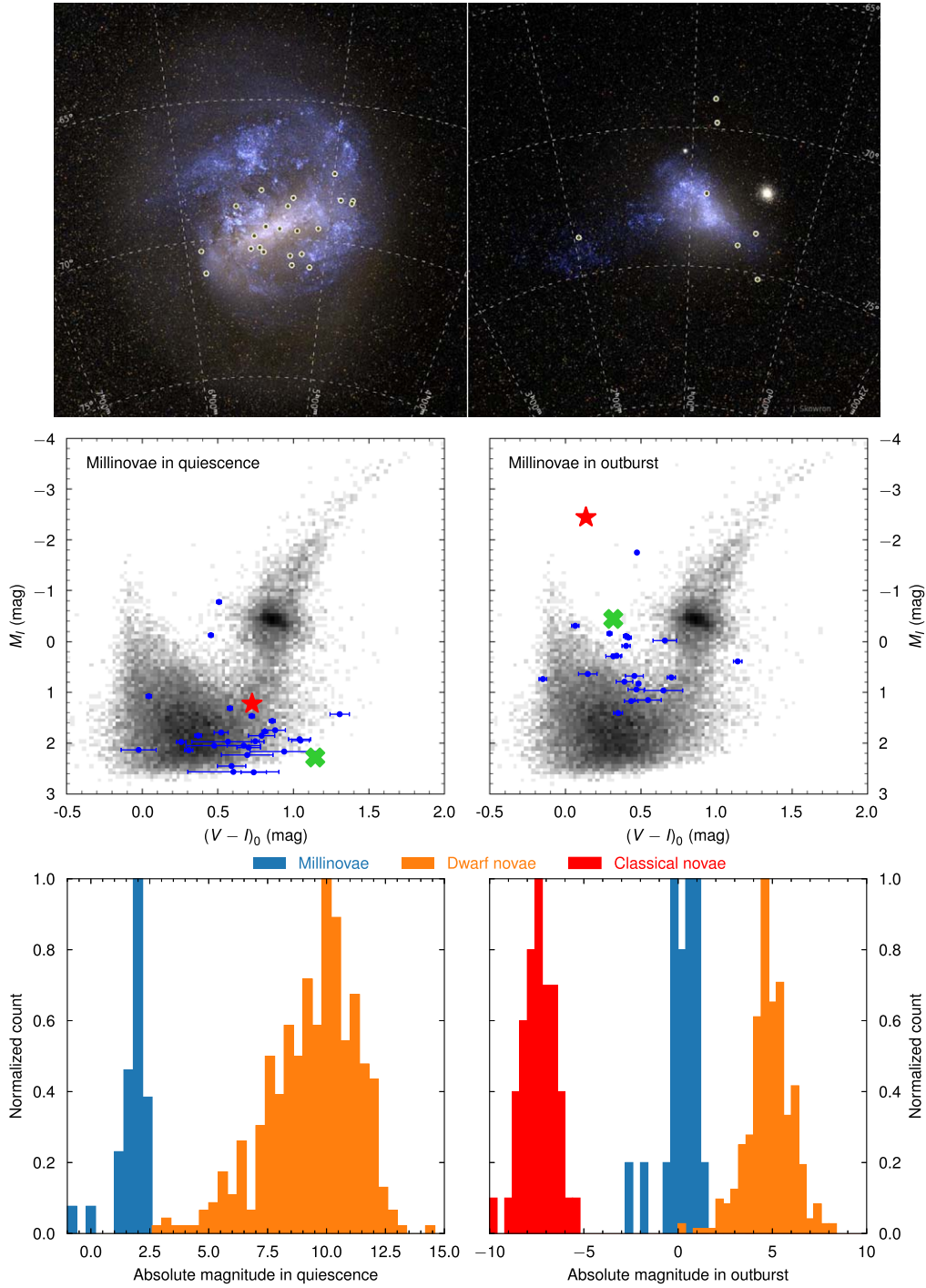


Figure 4. Upper panels: on-sky view of the LMC (upper left) and SMC (upper right) with positions of millinovae marked. Middle panels: dereddened color-magnitude diagrams for stars in the LMC. Blue points mark $(V - I_0)$ and M_I of millinovae in quiescence (middle left) and in outburst (middle right). The prototype, ASASSN-16oh, is marked with a red asterisk, and OGLE-mNOVA-11 is marked with a green cross. Lower panels: histograms of M_I of millinovae, classical novae, and dwarf novae in quiescence (lower left) and in outburst (lower right). Data were taken from H. Ritter & U. Kolb (2003), W. Pietsch (2010), and Gaia Collaboration et al. (2023). The background images of the LMC and SMC were generated with BSRENDER written by Kevin Loch, using the ESA/Gaia database.

OGLE-mNOVA-11 indicate that their optical outbursts likely have a disk origin. Because dwarf novae follow a well-known relation between the orbital period and absolute magnitude (both in quiescence and outburst; J. Patterson 2011), relatively high absolute magnitudes of millinovae indicate that their orbital periods should be on the order of a few days. Indeed, one of the analyzed objects (OGLE-mNOVA-08) shows clear eclipsing variability with a 4.830893(47) day period (Figure 5).

(We searched for possible periodic brightness variations in quiescence and during outbursts in all 29 objects but detected a statistically significant signal only in the case of OGLE-mNOVA-08.)

Furthermore, the rate of decline from the outburst of dwarf novae, τ_d , is also known to be proportional to P_{orb} (the “Bailey relation”; J. Bailey 1975; see Figure 6), as expected, given that longer periods imply larger disks. We find that most millinovae

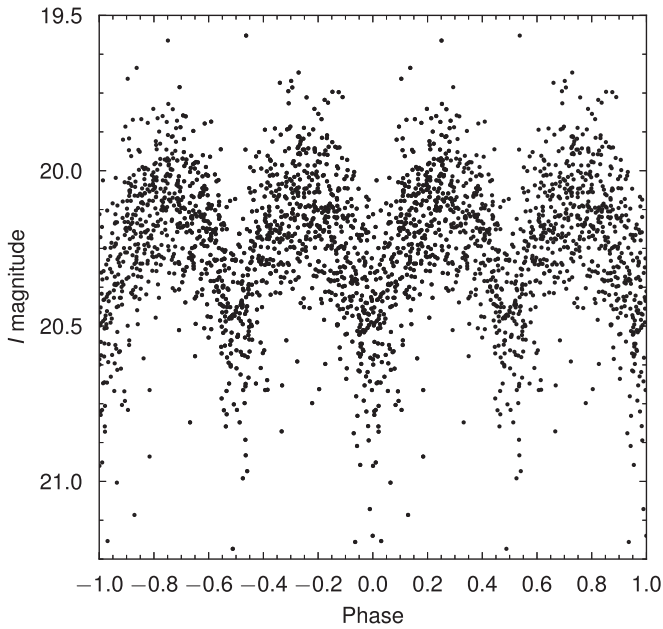


Figure 5. Quiescent light curve of OGLE-mNOVA-08 folded with the orbital period $P_{\text{orb}} = 4.830893$ days.

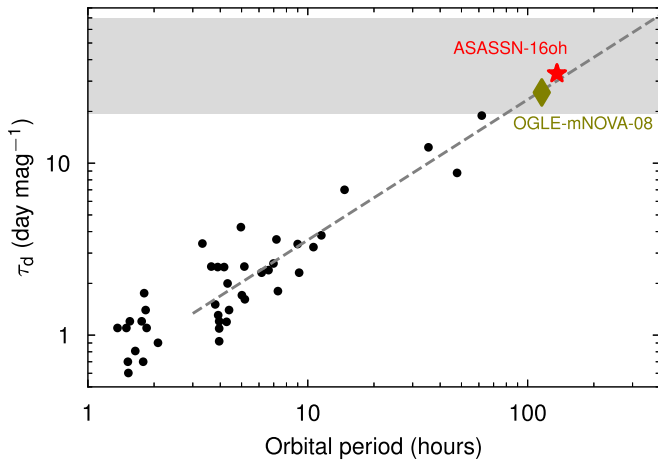


Figure 6. Orbital period (P_{orb})–decline rate (τ_d) relation for dwarf nova outbursts, using data from V. Simon (2021), and extended to include the range of decline rates (gray area) observed in millinovae ($20 \lesssim \tau_d \lesssim 70 \text{ day mag}^{-1}$). The red asterisk and green diamond mark the locations of ASASSN-16oh (A. Rajoelimanana et al. 2017) and OGLE-mNOVA-08, respectively.

have decline rates in the range $20 < \tau_d < 70 \text{ day mag}^{-1}$, which corresponds to P_{orb} from 3 to 15 days, assuming that the Bailey relation can be extrapolated to such long periods.

The “spreading layer” (R. Kippenhahn & H. C. Thomas 1978; N. A. Inogamov & R. A. Sunyaev 1999; A. L. Piro & L. Bildsten 2004; T. J. Maccarone et al. 2019) model can naturally produce the soft X-ray temperatures that have been seen in many dwarf nova outbursts, albeit in shorter-period systems such as U Gem and SS Cyg (see, e.g., P. J. Wheatley et al. 2003). However, the long orbital periods of millinovae imply the existence of large disks and hence likely large mass-transfer rates (e.g., J. Echevarria 1994) capable of producing higher X-ray luminosities. Nevertheless, there are difficulties with this model that have been noted (e.g., M. Kato et al. 2020) in that there are high mass-transfer-rate recurrent novae in quiescence (e.g., U Sco, RS Oph) where such a soft component would have been expected but has never been seen.

The most obvious solution to explaining the properties of millinovae is then to find a way to trigger thermonuclear burning on the white dwarf surface without producing a nova flash. One such attempt to do this is the nonejecting thermonuclear runaway event of Y. Hillman et al. (2019), but the resulting light curves of their ASASSN-16oh model are completely different to the smooth rise and fall that are observed, not to mention the huge color variation they predict, which is definitely excluded by the data.

An alternative route to such a trigger has been sought by M. Kato et al. (2020), who build on the already known, ongoing high mass-transfer rate in these systems (their brightness and variability properties are consistent with nova-like in the Magellanic Clouds; M. M. Shara et al. 2003), thereby keeping the disk (and white dwarf) in a hot, active state. Furthermore, they require a massive white dwarf, close to $1.2 M_{\odot}$ in order to initiate steady burning without a strong wind or shell being ejected. While we do not yet know how many of these long symmetric outburst systems produce detectable supersoft X-rays, if they were all to do so, then this would have important implications for the theory of nonejecting supersoft X-ray sources, as it would constrain the parameters of systems capable of behaving in this way. Furthermore, it would provide a route for allowing the white dwarf to continue to grow in mass and hence become a potential Type Ia supernova progenitor.

We recognize, however, that an added complication to the M. Kato et al. (2020) models is that they produce close to Eddington-limited events, whereas some of our millinovae clearly do not reach such a level in X-rays (Appendix E). There may be severe geometrical constraints on the fluxes observed, or the nuclear burning might not cover the entire white dwarf surface. Moreover, some of these models (see also M. Kato et al. 2022) predict the highest, close-to-Eddington flux to be in the far-UV range (rather than soft X-rays), which can be tested with dedicated follow-up observations of future millinova outbursts. Nevertheless, we believe that this new group of millinovae, all likely representing long-period, high mass-transfer-rate cataclysmic variables, opens an important new route for study, with the added benefit of being a well-constrained population in the Magellanic Clouds.

Acknowledgments

We thank all the OGLE observers for their contribution to the collection of the photometric data over the decades. This research was funded in part by National Science Centre, Poland, grant OPUS 2021/41/B/ST9/00252 awarded to P.M. K.L.P. acknowledges funding from the UK Space Agency. A part of this work is based on observations made with the Southern African Large Telescope (SALT), with the Large Science Programme on transients 2021-2-LSP-001 (PI: D.A.H.B.). Polish participation in SALT was funded by grant No. MEiN 2021/WK/01.

Facility: OGLE, Swift, SALT, eROSITA.

Appendix A Light Curves

Figures A1 and A2 show the light curves of the remaining stars exhibiting long-duration symmetrical outbursts, which we have classified as “millinovae.”

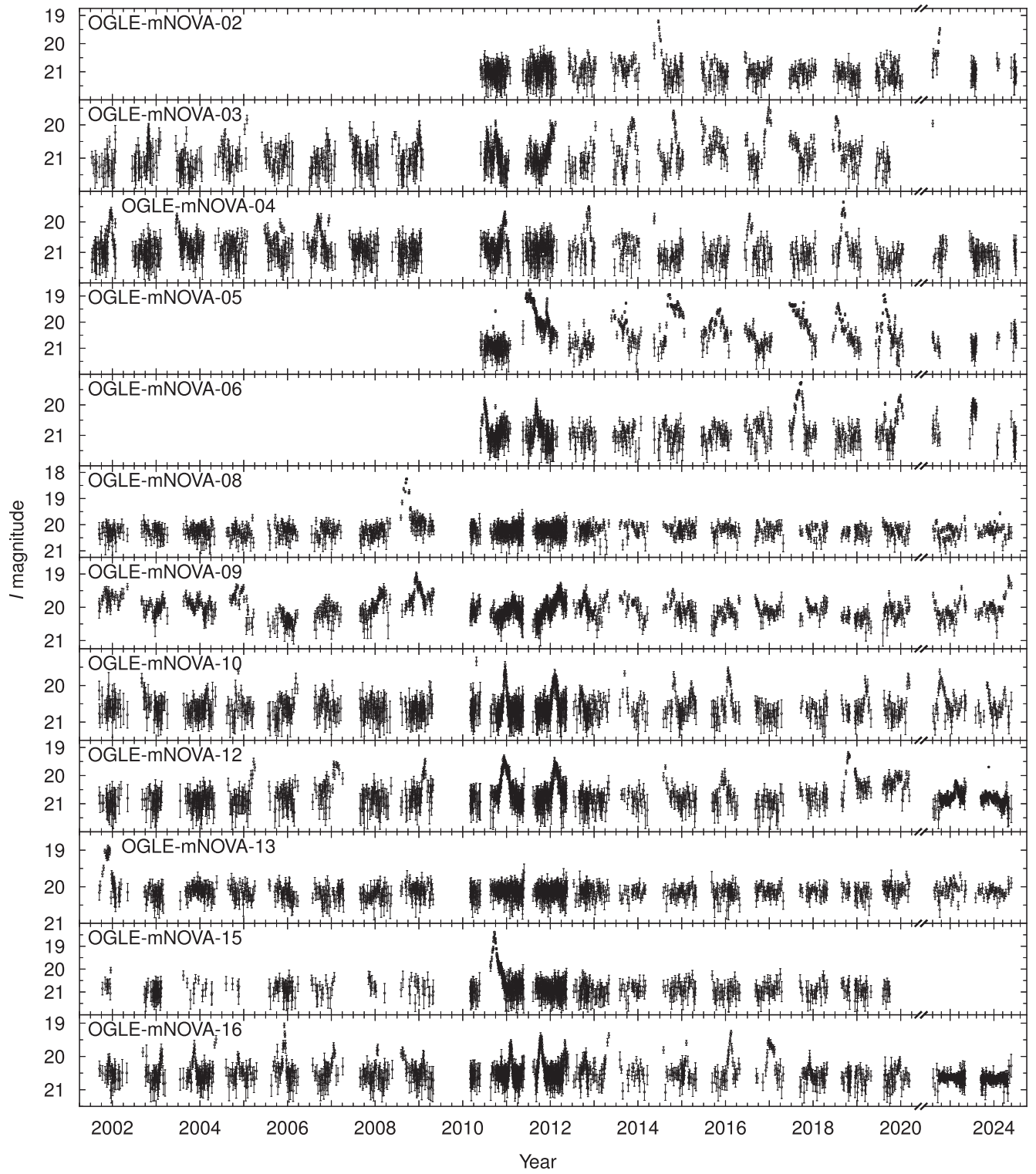


Figure A1. Example light curves of millinovae (continuation of Figure 1).

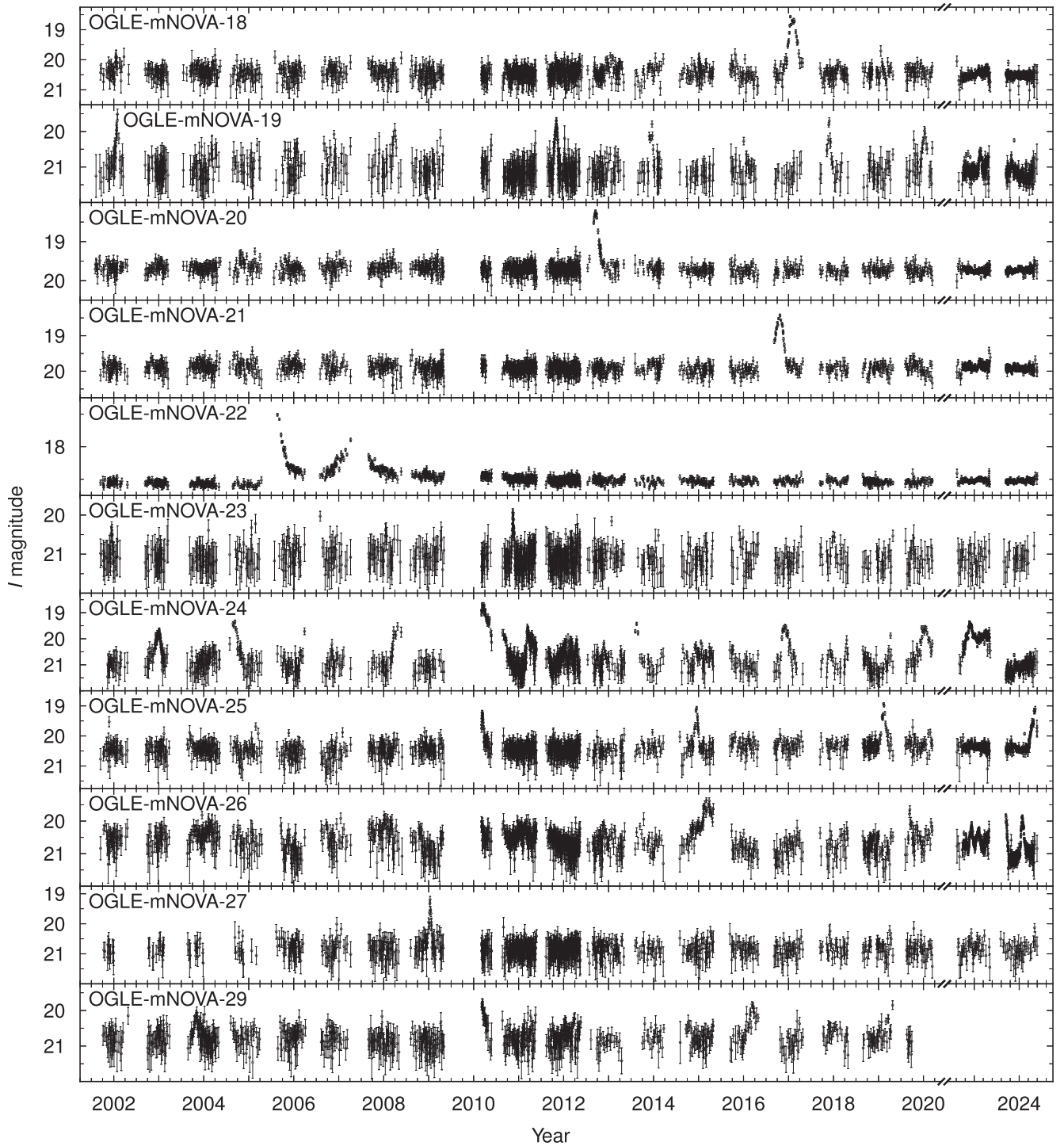


Figure A2. Example light curves of millinovae (continuation of Figure 1).

Appendix B

SALT Observations of OGLE-mNOVA-11

Optical spectra of OGLE-mNOVA-11 were obtained with the Robert Stobie Spectrograph (H. A. Kobulnicky et al. 2003; E. B. Burgh et al. 2003) mounted on SALT (D. A. H. Buckley et al. 2006) in long-slit mode. Two 1200 s exposure spectra were taken each night on 2023 November 22 and December 2, 3, 6, 8, and 10, using the PG0700 grating at an angle of 3° with a slit width of $1''.5$, giving a resolving power of $460 < R < 800$. The data were prereduced using the PySALT package

(S. M. Crawford et al. 2010), which includes bias subtraction, gain and cross-talk corrections, and mosaicking. An Argon lamp was utilized for wavelength calibration, and the spectrophotometric standard star, EG 21, was used for flux calibration, both performed with IRAF. The spectra were stacked so as to obtain one average spectrum per night.

The software package, Fityk¹² (M. Wojdyr 2010), was used for spectral analysis. The SALT spectra were normalized

¹² <https://fityk.nieto.pl/>

Table B1
SALT Radial Velocities of OGLE-mNOVA-11

Time	BJD	He II (km s ⁻¹)	H β (km s ⁻¹)	H α (km s ⁻¹)	Mean RV (km s ⁻¹)
2023 Nov 22.93	2460271.43	313.7 \pm 25.7	199.9 \pm 132.0	310.9 \pm 11.7	311.3 \pm 10.6
2023 Dec 2.88	2460281.38	308.5 \pm 8.6	329.4 \pm 25.6	306.7 \pm 18.2	308.2 \pm 7.8
2023 Dec 3.84	2460282.34	203.0 \pm 15.3	203.0 \pm 99.5	279.8 \pm 18.4	234.3 \pm 11.8
2023 Dec 6.84	2460285.34	224.1 \pm 19.1	475.5 \pm 95.5	252.8 \pm 30.9	232.1 \pm 16.3
2023 Dec 8.83	2460287.33	284.2 \pm 22.3	143.1 \pm 59.5	241.8 \pm 22.7	263.4 \pm 15.9
2023 Dec 10.83	2460289.33	245.2 \pm 13.4	417.6 \pm 124.2	257.4 \pm 19.7	249.0 \pm 11.1

before the emission lines were modeled using the method of A. W. Shafter (1983) in order to determine the central wavelengths of the He II (4686 Å), H β , and H α emission lines.. This entailed fitting a Gaussian function through 95% of the line wings. In Fityk, the errors of the fitted parameters were obtained for a confidence level of 1σ (68.27%). The measured central wavelengths were then utilized to calculate the barycentric-corrected radial velocities.

Table B1 presents the barycentric radial velocities of He II (4686 Å), H β , and H α . Because of the larger scatter in our H β velocities (due to its lower-significance detections), we also calculated the weighted mean radial velocity from He II and H α , obtaining values that ranged from 232.1 to 311.3 km s⁻¹, with a mean of 278.3 ± 4.5 km s⁻¹, which is very close to the established LMC line-of-sight velocity (262.2 ± 3.4 km s⁻¹; R. P. van der Marel et al. 2002). The number of radial velocity measurements prevents us from determining the orbital period unequivocally, but it is likely to be shorter than 4 days. If we restrict orbital periods to be longer than 1 day and assume a circular orbit, the best-fit periods are 2.42, 1.68, 2.08, and 1.89 days.

Appendix C

Swift Observations of OGLE-mNOVA-11

C.1 Swift X-Ray Data

The Neil Gehrels Swift Observatory (N. Gehrels et al. 2004) performed five Target of Opportunity observations of OGLE-mNOVA-11 (Target ID 16408) between 2023 December 6 and December 30, collecting ≈ 1.5 ks during each pointing, with the exception of December 17, when only ≈ 0.5 ks was obtained. The XRT (D. N. Burrows et al. 2005) was operated in photon counting mode, and the data were processed using HEASoft 6.32, together with the most up-to-date calibration files available. Given the faintness of the source, a small extraction region of 10 pixels (23''6) radius was used for the source, and a larger, 60 pixel (141''4) radius circle, offset from, but close to, the source was used to estimate the background contribution.

In observations where the source was detected at the 3σ level, the 0.3–10 keV count rate (corrected for all point-spread function losses) is given in Table C1. In the shorter exposure on December 17, the source was not detected, and a 3σ upper limit is given instead.

There is no significant change in the hardness ratio during these observations though it should be noted that we are dealing with a limited number of source counts (<50 in total across all five observations, the vast majority below 1 keV). Therefore, all the data were combined to create a single spectrum. Cash statistics (W. Cash 1979) were used to fit this spectrum with a combination of an optically thick blackbody for the soft emission and an optically thin thermal plasma to

Table C1
Swift XRT Observations of OGLE-mNOVA-11

Obs. ID	Start Time (UT)	Exp. Time (s)	Count Rate (10 ⁻³ s ⁻¹)
00016408001	2023-12-06 16:04:57	1594	11^{+3}_{-2}
00016408002	2023-12-13 09:21:57	1499	8 ± 2
00016408003	2023-12-17 07:10:56	479	< 20
00016408004	2023-12-20 04:27:56	1605	11 ± 2
00016408005	2023-12-30 16:46:56	1529	4^{+2}_{-1}

account for the few higher-energy photons, both absorbed by the same hydrogen column. While the optically thin plasma can only be constrained to have a temperature of >4.2 keV ($>4.9 \times 10^7$ K), the best-fitting blackbody temperature is 36^{+19}_{-25} eV ($418,000^{+220,000}_{-290,000}$ K), absorbed by a column density of $N_H = (3.5^{+13.0}_{-3.0}) \times 10^{21}$ cm⁻². This fit results in a C-stat value of 19.9 for 25 degrees of freedom.

If N_H is fixed to the LMC value of 1.3×10^{21} cm⁻² (HI4PI Collaboration et al. 2016), the blackbody temperature becomes slightly better constrained, with $kT = 52^{+14}_{-11}$ eV ($T = 607,000^{+160,000}_{-130,000}$ K), for C-stat/degrees of freedom = 21.2/26. This fit leads to an L_X (0.3–10 keV) of 9.0×10^{34} erg s⁻¹, or 3.6×10^{35} erg s⁻¹ unabsorbed (assuming a distance of 49.59 kpc; G. Pietrzyński et al. 2019).

C.2 Swift UV Data

OGLE-mNOVA-11 was also observed by the Ultraviolet and Optical Telescope (UVOT; P. W. A. Roming et al. 2005) on board the Neil Gehrels Swift Observatory. Observations took place during a period when one of the three onboard gyroscopes malfunctioned, resulting in increased noise and affecting the image quality of UVOT data (B. Cenko 2023). Moreover, the nearest source detected in the UVOT images was slightly offset from the target position by 3''6–4''8 and was likely a blend of the target and a nearby (5''4) bright ($V = 16.996$, $V - I = -0.097$) constant star. We measured the brightness of the blend using the UVOTSOURCE tool, which performs aperture photometry. We used an aperture with a radius of 15'' centered on the position of OGLE-mNOVA-11.

We then estimated the brightness of the neighbor from the analysis of the UV–optical color–magnitude diagrams, assuming that the neighbor's color is consistent with colors of other main-sequence stars of similar magnitude. We, therefore, created UV–optical color–magnitude diagrams by cross-matching the UVOT catalogs with the OGLE photometric map. We then calculated the mean $UV - V$ color of main-sequence stars in the brightness range $|V - 16.996| < \Delta$, where

Table C2
Swift UVOT Observations of OGLE-mNOVA-11

Obs. ID	<i>uvw1</i>	<i>uvm2</i>	<i>uvw2</i>
00016408001	...	15.838 ± 0.046	...
00016408002	16.448 ± 0.094	16.042 ± 0.078	16.019 ± 0.068
00016408003	...	15.843 ± 0.068	...
00016408004	...	16.166 ± 0.059	...
00016408005	...	16.197 ± 0.074	...

$\Delta = 0.15$ mag. We found

$$uvm2 - V = -1.462 \pm 0.078,$$

$$uvw1 - V = -1.482 \pm 0.064,$$

$$uvw2 - V = -1.559 \pm 0.077.$$

(We also tested $\Delta = 0.1$ and $\Delta = 0.2$ and obtained similar results.) That enabled us to estimate the brightness of the neighbor in the UV filters:

$$uvm2 = 15.534 \pm 0.078,$$

$$uvw1 = 15.514 \pm 0.064,$$

$$uvw2 = 15.437 \pm 0.077$$

and estimate the UV brightness of the target by subtracting the brightness of the neighbor star. Results are reported in Table C2. All magnitudes are in the Vega system.

Appendix D OGLE Proper Motions

We calculated the proper motions of detected stars using the OGLE time-series astrometric data (OGLE-Uranus; A. Udalski et al. 2024, in preparation). In short, we measured each star's position (x , y) in individual OGLE images collected between 2010 and 2024 (in some cases, 2010–2020 if later data were unavailable). We then cross-matched the positions of bright stars with those calculated using the Gaia DR3 data (Gaia Collaboration et al. 2016, 2023), taking into account their proper motion and heliocentric parallax. That allowed us to find the transformation between the positions (x , y) in individual OGLE images to the equatorial coordinates in the Gaia reference frame (L. Lindegren et al. 2021). The proper motions in R.A. μ_α and decl. μ_δ for all detected stars are reported in Table D1. Because most of our targets are very faint ($I \approx 20$ –21), the proper motion uncertainties are large (the median error bar is 2 mas yr^{−1}). Nonetheless, in all cases (but one), the proper motions are consistent within the quoted errors with the Magellanic Clouds' proper motions (Gaia Collaboration et al. 2018). The only exception is OGLE-mNOVA-15 with a total proper motion of 23.5 ± 3.8 mas yr^{−1}, making it most likely to be a foreground object, and we therefore treat it as a candidate millinova.

Table D1
Millinovae Proper Motions

Object	μ_α (OGLE) (mas yr ^{−1})	μ_δ (OGLE) (mas yr ^{−1})	μ_α (Gaia) (mas yr ^{−1})	μ_δ (Gaia) (mas yr ^{−1})
OGLE-mNOVA-01	1.66 ± 2.03	0.14 ± 2.39
OGLE-mNOVA-02	1.31 ± 2.35	−2.50 ± 2.31
OGLE-mNOVA-03	1.60 ± 3.22	−4.03 ± 2.68
OGLE-mNOVA-04	1.25 ± 2.78	−3.15 ± 2.53
OGLE-mNOVA-05	−0.37 ± 1.44	−0.44 ± 1.49	0.55 ± 0.51	−1.19 ± 0.65
OGLE-mNOVA-06	−0.67 ± 2.04	0.29 ± 2.16
OGLE-mNOVA-07	0.74 ± 0.09	−1.39 ± 0.10	0.80 ± 0.17	−1.18 ± 0.18
OGLE-mNOVA-08	0.85 ± 0.91	0.84 ± 0.92
OGLE-mNOVA-09	−1.26 ± 1.16	0.08 ± 1.16
OGLE-mNOVA-10	2.13 ± 1.26	−0.13 ± 1.51
OGLE-mNOVA-11	4.35 ± 2.18	4.08 ± 2.37
OGLE-mNOVA-12	−3.00 ± 2.51	−7.29 ± 2.64
OGLE-mNOVA-13	2.11 ± 0.74	−0.25 ± 0.66	2.53 ± 2.28 ^a	10.09 ± 2.60 ^a
OGLE-mNOVA-14	1.96 ± 2.56	−2.29 ± 1.99
OGLE-mNOVA-15	12.35 ± 3.04	−20.00 ± 4.11
OGLE-mNOVA-16	3.32 ± 1.37	−9.88 ± 3.42
OGLE-mNOVA-17	1.44 ± 1.32	2.71 ± 1.87
OGLE-mNOVA-18	0.91 ± 1.40	0.38 ± 1.67
OGLE-mNOVA-19	−4.35 ± 3.39	−1.48 ± 2.37
OGLE-mNOVA-20	−0.34 ± 1.67	1.88 ± 0.51
OGLE-mNOVA-21	0.19 ± 0.61	0.02 ± 0.68
OGLE-mNOVA-22	1.82 ± 0.09	0.71 ± 0.10	2.24 ± 0.19	1.16 ± 0.24
OGLE-mNOVA-23	−1.93 ± 4.22	3.85 ± 6.32
OGLE-mNOVA-24	6.43 ± 4.11	1.45 ± 2.32
OGLE-mNOVA-25	−0.27 ± 2.01	−0.13 ± 2.81
OGLE-mNOVA-26	4.13 ± 1.71	1.49 ± 0.97
OGLE-mNOVA-27	−0.33 ± 1.44	3.21 ± 2.41
OGLE-mNOVA-28	−1.22 ± 2.05	0.05 ± 1.94
OGLE-mNOVA-29	−1.85 ± 2.75	−0.54 ± 2.33

Note.

^a The Gaia DR3 (Gaia Collaboration et al. 2016, 2023) astrometric solution is unreliable because the renormalized unit weight error is larger than 1.4 (L. Lindegren et al. 2021).

Appendix E



eROSITA Upper Limits















The first catalog of X-ray sources detected by the eROSITA telescope array (P. Predehl et al. 2021) on board the Spectrum-Roentgen-Gamma (SRG; R. Sunyaev et al. 2021) satellite was recently published by A. Merloni et al. (2024). The number of exposures, and so the depth of the survey, depends on sky position. Thanks to the SRG scanning law, objects located near the ecliptic poles are observed most frequently. Coincidentally, the LMC is located near the south ecliptic pole.

We cross-matched our list with the eROSITA catalog (A. Merloni et al. 2024), but none of the objects from Table 1 were detected by eROSITA. The catalog of A. Merloni et al. (2024) contains X-ray sources located in the western Galactic hemisphere detected during the first 6 months of eROSITA operations (from 2019 December 12 to 2020 June 11, that is, $2,458,829 < \text{JD} < 2,459,011$). The overlap with OGLE observations is relatively small because the OGLE-IV operations were suspended on 2020 March 18 (JD = 2,458,927) due to the COVID-19 pandemic. Nonetheless, we found that four objects (OGLE-mNOVA-06, OGLE-mNOVA-10, OGLE-mNOVA-19, and OGLE-mNOVA-24) were in outburst during the first eROSITA All-Sky Survey. All four objects were relatively faint and reached a peak $I \sim 19.55\text{--}19.98$ during that time. Assuming that the X-ray flux scales proportionally with peak I -band flux, and taking OGLE-mNOVA-11 as a benchmark, the maximal expected X-ray flux is $\sim (6\text{--}8) \times 10^{-14} \text{ erg cm}^{-2} \text{ s}^{-1}$ in the 0.3–10 keV range. The expected flux in the eROSITA soft and medium energy bands (0.2–2.3 keV) is about 6% larger at $(6\text{--}9) \times 10^{-14} \text{ erg cm}^{-2} \text{ s}^{-1}$. However, each object must have been scanned by eROSITA multiple times, and the time-averaged flux is likely to be smaller.

We queried the eROSITA upper limits service (M. Krumpe et al. 2024) to get upper flux limits in the 0.2–2.3 keV range for all four objects discussed above. These limits are calculated at a 99.87% (3σ) one-sided confidence level, assuming a power-law spectrum with a photon index $\Gamma = 2.0$ and a column density $N_{\text{H}} = 3 \times 10^{20} \text{ cm}^{-2}$. We obtained limits of $(5.1, 1.9, 2.0, 3.8) \times 10^{-14} \text{ erg cm}^{-2} \text{ s}^{-1}$ at the positions of OGLE-mNOVA-(06, 10, 19, 24), respectively. We followed a procedure outlined in M. Krumpe et al. (2024) to estimate upper limits for the best-fitting absorbed blackbody model presented in Appendix C. Using the appropriate eROSITA calibration files and XSPEC version 12.14.0 (K. A. Arnaud 1996), we estimated the energy-to-count conversion factor of $1.037 \times 10^{12} \text{ cm}^2 \text{ erg}^{-1}$, which is only 3.4% smaller than that calculated using the fiducial model in M. Krumpe et al. (2024). Therefore, the upper limits for our best-fitting model are only 3.4% larger than default ones. In the 0.2–5 keV range, the corresponding limits are $(7.5, 3.7, 2.5, 5.4) \times 10^{-14} \text{ erg cm}^{-2} \text{ s}^{-1}$. We thus conclude that the expected time-averaged flux is close to or below the current eROSITA limits. It is therefore possible that the selected stars may be detected in future eROSITA data releases once more data are processed or may be detected in data from individual scans.

ORCID iDs

Przemek Mróz  <https://orcid.org/0000-0001-7016-1692>
 Krzysztof Król  <https://orcid.org/0009-0006-3777-6381>
 Hélène Szegedi  <https://orcid.org/0000-0002-9904-3582>
 Kim L. Page  <https://orcid.org/0000-0001-5624-2613>
 Andrzej Udalski  <https://orcid.org/0000-0001-5207-5619>

David A. H. Buckley  <https://orcid.org/0000-0002-7004-9956>
 Gulab Dewangan  <https://orcid.org/0000-0003-1589-2075>
 Michał K. Szymański  <https://orcid.org/0000-0002-0548-8995>
 Igor Soszyński  <https://orcid.org/0000-0002-7777-0842>
 Paweł Pietrukowicz  <https://orcid.org/0000-0002-2339-5899>
 Szymon Kozłowski  <https://orcid.org/0000-0003-4084-880X>
 Radosław Poleski  <https://orcid.org/0000-0002-9245-6368>
 Jan Skowron  <https://orcid.org/0000-0002-2335-1730>
 Krzysztof Ulaczyk  <https://orcid.org/0000-0001-6364-408X>
 Mariusz Gromadzki  <https://orcid.org/0000-0002-1650-1518>
 Krzysztof Rybicki  <https://orcid.org/0000-0002-9326-9329>
 Patryk Iwanek  <https://orcid.org/0000-0002-6212-7221>
 Marcin Wrona  <https://orcid.org/0000-0002-3051-274X>
 Mateusz J. Mróz  <https://orcid.org/0000-0002-8911-6581>

References

- Alard, C., & Lupton, R. H. 1998, *ApJ*, **503**, 325
 Alcock, C., Allsman, R. A., Alves, D. R., et al. 2000, *ApJ*, **542**, 281
 Arnaud, K. A. 1996, in ASP Conf. Ser. 101, *Astronomical Data Analysis Software and Systems V*, ed. G. H. Jacoby & J. Barnes (San Francisco, CA: ASP), 17
 Bailey, J. 1975, *JBA*, **86**, 30
 Bode, M. F., & Evans, A. 2008, *Classical Novae*, Vol. 43 (2nd edn.; Cambridge: Cambridge Univ. Press)
 Buckley, D. A. H., Swart, G. P., & Meiring, J. G. 2006, *Proc. SPIE*, **6267**, 62670Z
 Burgh, E. B., Nordsieck, K. H., & Kobulnicky, H. A. 2003, *Proc. SPIE*, **4841**, 1463
 Burrows, D. N., Hill, J. E., Nousek, J. A., et al. 2005, *SSRv*, **120**, 165
 Cash, W. 1979, *ApJ*, **228**, 939
 Cenko, B. 2023, *GCN*, **34633**, 1
 Crawford, S. M., Still, M., & Schellart, P. 2010, *Proc. SPIE*, **7737**, 773725
 Echevarria, J. 1994, *RMxAA*, **28**, 125
 Gaia Collaboration, Helmi, A., van Leeuwen, F., et al. 2018, *A&A*, **616**, A12
 Gaia Collaboration, Prusti, T., de Bruijne, J. H. J., et al. 2016, *A&A*, **595**, A1
 Gaia Collaboration, Vallenari, A., Brown, A. G. A., et al. 2023, *A&A*, **674**, A1
 Gehrels, N., Chincarini, G., Giommi, P., et al. 2004, *ApJ*, **611**, 1005
 Graczyk, D., Pietrzyński, G., Thompson, I. B., et al. 2020, *ApJ*, **904**, 13
 Henze, M., Pietsch, W., Haberl, F., et al. 2014, *A&A*, **563**, A2
 HI4PI Collaboration, Ben Bekhti, N., Flöer, L., et al. 2016, *A&A*, **594**, A116
 Hillman, Y., Orto, M., Prialnik, D., et al. 2019, *ApJL*, **879**, L5
 Inogamov, N. A., & Sunyaev, R. A. 1999, *AstL*, **25**, 269
 Kato, M., Saio, H., & Hachisu, I. 2020, *ApJ*, **892**, 15
 Kato, M., Saio, H., & Hachisu, I. 2022, *PASJ*, **74**, 1005
 Kippenhahn, R., & Thomas, H. C. 1978, *A&A*, **63**, 265
 Kobulnicky, H. A., Nordsieck, K. H., & Burgh, E. B. 2003, *Proc. SPIE*, **4841**, 1634
 Lasota, J.-P. 2001, *NewAR*, **45**, 449
 Lindegren, L., Klioner, S. A., Hernández, J., et al. 2021, *A&A*, **649**, A2
 Maccarone, T. J., Nelson, T. J., Brown, P. J., et al. 2019, *NatAs*, **3**, 173
 Merloni, A., Lamer, G., Liu, T., et al. 2024, *A&A*, **682**, A34
 Mróz, P., Udalski, A., Szymański, M. K., et al. 2024, *ApJS*, **273**, 4
 Osborne, J. P. 2015, *JHEAp*, **7**, 117
 Page, K. L., & Shaw, A. W. 2022, in *Handbook of X-Ray and Gamma-Ray Astrophysics*, ed. C. Bambi & A. Sanganello (Singapore: Springer), 107
 Patterson, J. 2011, *MNRAS*, **411**, 2695
 Pietrzyński, G., Graczyk, D., Galloway, A., et al. 2019, *Natur*, **567**, 200
 Pietsch, W. 2010, *AN*, **331**, 187
 Piro, A. L., & Bildsten, L. 2004, *ApJ*, **610**, 977
 Predehl, P., Andritschke, R., Arefiev, V., et al. 2021, *A&A*, **647**, A1
 Rajoelimanana, A., Charles, P., Buckley, D., & Meintjes, P. 2017, in 5th Annual Conf. on High Energy Astrophysics in Southern Africa ed. P. Meintjes, 3
 Ritter, H., & Kolb, U. 2003, *A&A*, **404**, 301
 Rodriguez, A. C., El-Badry, K., Suleimanov, V., et al. 2024, arXiv:2408.16053
 Roming, P. W. A., Kennedy, T. E., Mason, K. O., et al. 2005, *SSRv*, **120**, 95
 Scaringi, S., Groot, P. J., Knigge, C., et al. 2022, *Natur*, **604**, 447
 Schwöpe, A. D., Knauff, K., Kurpas, J., et al. 2024, *A&A*, **690**, A243
 Shafter, A. W. 1983, *ApJ*, **267**, 222
 Shappee, B. J., Prieto, J. L., Grupe, D., et al. 2014, *ApJ*, **788**, 48
 Shara, M. M., Hinkley, S., & Zurek, D. R. 2003, *AJ*, **126**, 2887

- Simon, V. 2021, in *The Golden Age of Cataclysmic Variables and Related Objects V*, 2, ed. F. Giovannelli (Trieste: SISSA), [37](#)
- Skowron, D. M., Skowron, J., Udalski, A., et al. 2021, [ApJS](#), **252**, [23](#)
- Sunyaev, R., Arefiev, V., Babyshkin, V., et al. 2021, [A&A](#), **656**, [A132](#)
- Tomaney, A. B., & Crotts, A. P. S. 1996, [AJ](#), **112**, [2872](#)
- Tubín-Arenas, D., Krumpe, M., Lamer, G., et al. 2024, [A&A](#), **682**, [A35](#)
- Udalski, A. 2003, *AcA*, **53**, [291](#)
- Udalski, A., Szymański, M. K., & Szymański, G. 2015, [AcA](#), **65**, [1](#)
- van der Marel, R. P., Alves, D. R., Hardy, E., & Suntzeff, N. B. 2002, [AJ](#), **124**, [2639](#)
- Wheatley, P. J., Mauche, C. W., & Mattei, J. A. 2003, [MNRAS](#), **345**, [49](#)
- Wojdyr, M. 2010, [JApCr](#), **43**, [1126](#)
- Woźniak, P. R. 2000, *AcA*, **50**, [421](#)
- Wyrzykowski, Ł., Kozłowski, S., Skowron, J., et al. 2009, [MNRAS](#), **397**, [1228](#)